Towards windproofing LIGO: Reducing the effect of wind-driven floor tilt by using rotation sensors in active seismic isolation.

Krishna Venkateswara[1], Michael P. Ross[1*], Jim Warner[2], Conor Mow-Lowry[3], Brian Lantz[4], Jeffrey Kissel[2] , Hugh Radkins[2], Thomas Shaffer[2], Richard Mittleman[5], Sam Cooper[3], Arnaud Pele[6], and Jens Gundlach[1]

E-mail: mpross2@uw.edu*
[1]Center for Experimental Nuclear Physics and Astrophysics, University of Washington, Seattle, Washington 98195, USA,
[2]LIGO Hanford Observatory, Richland, Washington 99352, USA,
[3]University of Birmingham, Birmingham B15 2TT, United Kingdom,
[4]Stanford University, Stanford, California 94305, USA,
[5]Massachusetts Institute of Technology, Cambridge, Massachusetts 02139, USA,
[6]LIGO Livingston Observatory, Livingston, Louisiana 70754, USA

Abstract. Modern gravitational-wave observatories require robust low-frequency active seismic isolation in order to keep the interferometer at ideal operating conditions. Seismometers are used to measure both the motion of the ground and isolated platform. These devices are susceptible to contamination from ground tilt at frequencies below 0.1 Hz, particularly arising from wind-pressure acting on building walls. Consequently, both LIGO observatories suffered significant downtime when wind-speeds were above 7 m/s during LIGO's first observation run. We describe the use of ground rotation sensors at LIGO Hanford Observatory to correct nearby ground seismometers to produce tilt-free ground displacement signals. The use of these signals for feedforward isolation enables a robust low-frequency seismic isolation. This allowed the observatory to operate under wind speeds as high as $15-20$ m/s during the second observation run.

PACS numbers: 07.10.Fq

Submitted to: *Class. Quantum Grav.*

1. Introduction

During the first observation run of the Advanced Laser Interferometer Gravitational-wave Observatory (LIGO), multiple gravitational-wave candidates were detected over a 16-week-long duration [1]. The duty-cycle of the LIGO Hanford Observatory (LHO) and the LIGO Livingston Observatory (LLO) was 67.6% and 57.4%, respectively, with significant downtime due to high wind and microseismic motion [2]. Even when the interferometers were operational, significant excess noise was observed in the detectors when wind-speeds exceeded 7 m/s.

To keep an interferometer locked and operating at it's optimum point, the net differential motion of the suspended test-masses in the two arm-cavities needs to be less than 10^{-14} m rms. The differential ground motion over the observatory's 4-km long arms has a strong frequency dependence and varies with time. Fig. 1 shows an example of the horizontal ground motion measured at LHO when the wind speeds were below 3 m/s. As will be seen later, wind-induced ground tilt can dominate the observed ground motion below 0.1 Hz due to tilt-contamination of seismometer readings. [3] These tilts arise from deformations of the observatory's floor due to wind-driven pressure fluctuations on the walls of the building. Between 0.05 to 0.5 Hz, the ground motion is largely dictated by Rayleigh waves arising from ocean waves interacting with the sea floor [4]. The $10-15$ second period ocean waves produce the so-called primary, secondary and tertiary microseism peaks through interference effects. The amplitude of the secondary is usually the largest and can vary from $\sim 0.1-3$ μm depending on ocean activity and location. It is also worth noting that the differential ground motion over the 4-km arm is reduced significantly between 0.05 to 0.2 Hz, due to the fact that the wavelength of the seismic waves at these frequencies is ~ 40 km. Additionally, at the diurnal and semi-diurnal frequency, the earth tides can produce between $100-250$ μm of differential displacement over the arms. To operate the interferometer in such an environment, multiple feedback loops are deployed to minimize the length and angular variations of the test mass cavities.

The data and analysis in this paper is limited to LHO, which was the only site that received tilt-sensors between the first (O1) and second (O2) observing runs. The

ground motion at the two LIGO sites are notably different (due to the location and ground properties) which makes it difficult to immediately apply the following control scheme to LLO. Nevertheless, similar schemes are deployed at LLO and could be applied to other terrestrial gravitational wave observatories.

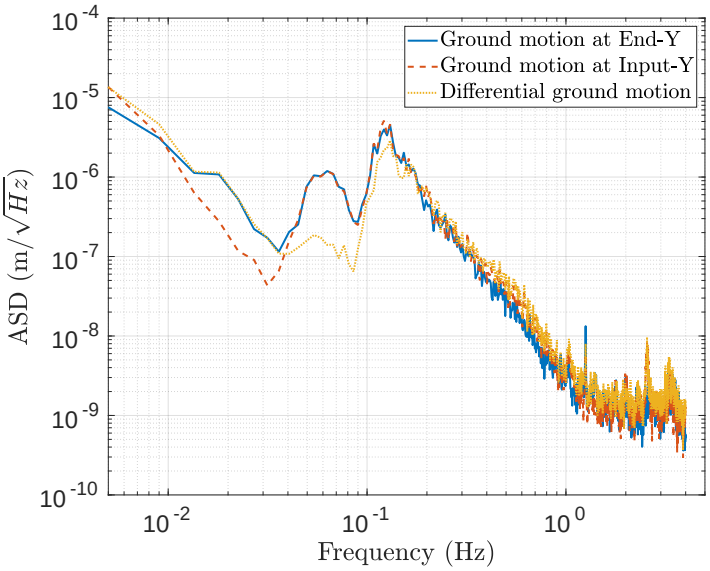

Figure 1. Amplitude spectral density (ASD) of the ground motion along the Y-arm at LHO, measured near the input (ITMY) and end (ETMY) test masses and the differential motion between the two. The primary and secondary microseismic peaks are clearly visible between 0.05 to 0.5 Hz.

1.1. Platform Control Configuration

The active isolation system in LIGO is described in detail in [5]. In general, the suspended platform can be controlled by feedback using on-board sensors or by feedforward using sensors on the ground. When viewed locally, these two approaches are nearly equivalent if the sensors are the same. However, using on-board sensors for feedback is slightly superior as the motion sensed at the ground and the motion affecting the platform may differ. In the first Observation run, only on-board sensors were used for feedback cancellation of the platform motion down to approximately 50 mHz, referred to as the O1 Configuration. After O1, two beam-rotation-sensors (BRS) [6] were installed at the end-stations of LHO and used to subtract the tilt-coupling of the ground seismometers [3]. The tilt sensed by the corner-station seismometer was significantly less than the end-station seismometers under similar wind-speeds. This is likely due to its location further from the building walls than is possible at the end-stations. Thus the tilt-subtracted seismometers at the end-stations and a tilt-free seismometer at the corner station form a set of low-tilt seismometers. For the second observing run, the strategy of using a combination of the low-tilt ground seismometers for feedforward at low frequencies (known as sensor correction) and on-board sensors

for feedback at high frequencies was adopted, referred to as the O2 Configuration.

The drawback of the O1 configuration is that it increased platform motion dramatically under windy conditions due to increased ground tilt. It also failed to take advantage of the correlated ground motion in the 50-150 mHz range over the 4-km arms and high correlation over the tens of meters separating the corner station chambers.

2. Simple Analytical Model

The active isolation of the LIGO test-masses employs two main subsystems- the Hydraulic External Pre-Isolation (HEPI) and the Internal Seismic Isolation (ISI). For a detailed description see [5]. The test mass ISI is a dual-stage actively-controlled isolation system from which the test mass assembly is suspended. The analytical model considered below describes the isolation achieved by the first stage of the ISI. This accounts for the majority of the low-frequency performance of the system. This calculation follows the procedure outlined in [7]. While this model lacks the full complexity and ability to incorporate cross-couplings of a numerical model, it is instructive in understanding the main features of the system and in guiding the development of feedforward filters.

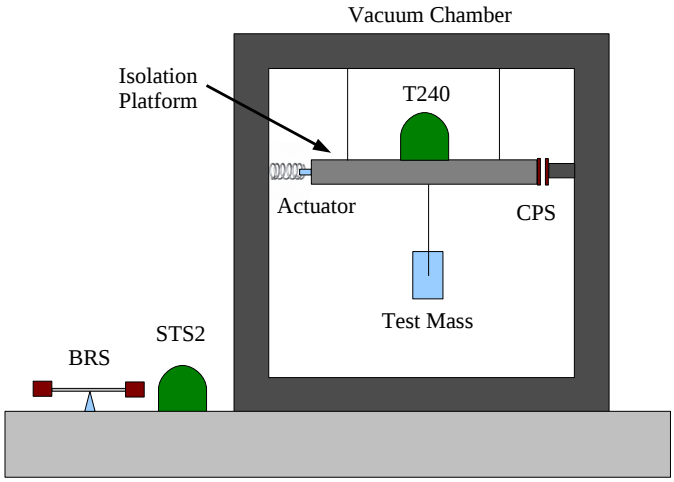

Figure 2. Schematic representation of the Internal Seismic Isolation platform.

Fig. 2 shows a simplified schematic of the ISI which includes the on-board seismometer (T240), capacitative position sensor (CPS), the ground seismometer (STS2), and the ground tilt-sensor (BRS). Fig. 3 and Fig. 4 show control loop diagrams for both the tilt and translation-degrees of freedom.

In the limit of large loop gains and at frequencies where the mechanical dynamics are unimportant, the equations governing the platform motion with a given ground motion, and sensor noises is shown in the following.

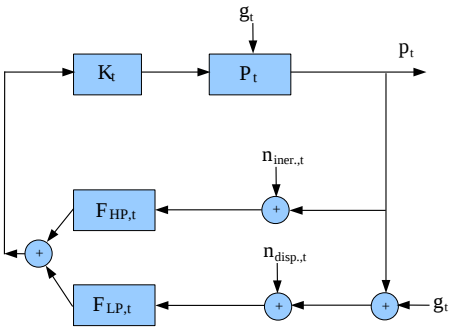

Figure 3. Model of the tilt control loop for the first stage of the ISI. Where g_t is the ground tilt, p_t is the platform tilt, $n_{iner.,t}$ and $n_{disp.,t}$ are the tilt sensor noises for the on-board T240 pair and position sensor respectively, $F_{HP,t}$ and $F_{LP,t}$ are respectively high pass and low pass filters, K_t is the feedback filter, and P_t is the platform tilt transfer function.

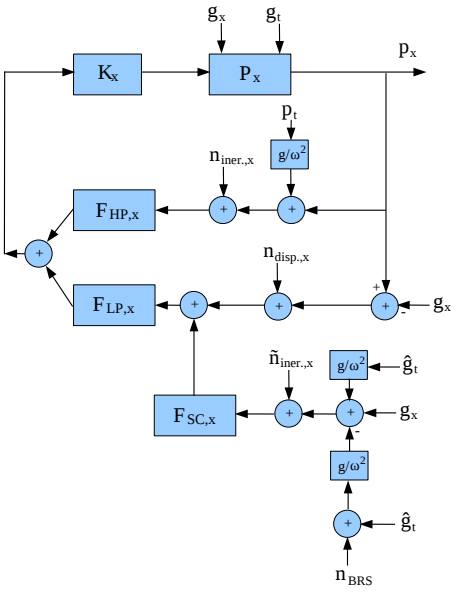

Figure 4. Model of the translation control loop for the first stage of the ISI. Where g_t, $\hat{g}_t$, and g_x are the ground tilt at the platform, ground tilt at the ground seismometer, and ground translation respectively, p_x and p_t are the platform translation and tilt, $n_{iner.,x}$, $\tilde{n}_{iner.,x}$, $n_{disp.,x}$ and n_{BRS} are the sensor noises for the on-board T240, ground STS2, position sensor, and BRS respectively, $F_{HP,x}$, $F_{LP,x}$, and $F_{SC,x}$ are respectively a high pass filter, a low pass filter, and the sensor correction filter, K_x is the feedback filter, and P_x is the platform translation transfer function.

The platform translations sourced by ground translations can be expressed as

$$p_x = F_{LP,x} \cdot (1 - F_{SC,x}) \cdot g_x. \tag{1}$$

Where g_x is the ground translation, p_x is the platform translation, $F_{LP,x}$ and $F_{SC,x}$ are respectively a low pass filter and the sensor correction filter.

Ground tilt can produce platform translation through the following two terms:

$$p_x = -F_{LP,x} \cdot F_{SC,x} \cdot \frac{g}{\omega^2} \cdot \hat{g}_t - F_{HP,x} \cdot \frac{g}{\omega^2} \cdot F_{LP,t} \cdot g_t. \tag{2}$$

Where g_t is the ground tilt at the platform, $\hat{g}_t$ is the ground tilt at the ground seismometer, p_x is the platform translation, $F_{HP,x}$, $F_{LP,x}$, and $F_{SC,x}$ are respectively a high pass filter, a low pass filter, and the sensor correction filter, g is the gravitational acceleration, and ω is the frequency of motion. The first term is due to the tilt-sensitivity of the ground seismometer while the second is due to the platform tilt being sensed as translation by the platform seismometer.

When a tilt sensor is used to subtract the tilt contamination from the ground sensor, the ground tilt in the first term is replaced with the level of noise in the tilt-subtracted channel. Ideally this would be dominated by the tilt sensor and the seismometer sensor noise. In reality, the tilt-subtracted residual signal is known to be limited by differences in tilt experienced by the two sensors. Hence a signal-dependent 'noise' is added to the tilt-subtracted channel. Therefore with the use of the BRS, eq. 2 is modified as follows:

$$p_x = -F_{LP,x} \cdot F_{SC,x} \cdot \frac{g}{\omega^2} \cdot n_{TS} - F_{HP,x} \cdot \frac{g}{\omega^2} \cdot F_{LP,t} \cdot g_t. \tag{3}$$

Where the noise in the tilt-subtracted channel n_{TS} is modelled as

$$n_{TS} = -n_{BRS} + \alpha \cdot \hat{g}_t \tag{4}$$

Where α is the residual tilt factor which in the current sensor scheme is $\sim \frac{1}{10}$.

The sum of sensor noises affecting the platform translation can be written as

$$\begin{aligned} p_x = & -F_{HP,x} \cdot n_{iner.,x} - F_{LP,x} \cdot n_{disp.,x} \\ & - F_{LP,x} \cdot F_{SC,x} \cdot \tilde{n}_{iner.,x} + F_{HP,x} \cdot \frac{g}{\omega^2} \cdot F_{HP,t} \cdot n_{iner.,t} \\ & + F_{HP,x} \cdot \frac{g}{\omega^2} \cdot F_{LP,t} \cdot n_{disp.,t} \end{aligned} \tag{5}$$

Where p_x is the platform translation, $n_{iner.,x}$, $\tilde{n}_{iner.,x}$, and $n_{disp.,x}$ are respectively the translation noise for the on-board T240, ground STS2, and CPS, $n_{iner.,t}$ and $n_{disp.,t}$ are the tilt noise for the on-board T240 pair and CPS respectively. Similarly, the platform tilt arising due to ground tilt is

$$p_t = F_{LP,t} \cdot g_t. \tag{6}$$

And the platform tilt due to the sum of sensor noises is

$$p_t = -F_{HP,t} \cdot n_{iner.,t} - F_{LP,t} \cdot n_{disp.,t}. \tag{7}$$

To study the effects of different filters configurations, we construct an idealized model of both the translation and tilt inputs to the system. Fig. 5 shows the Amplitude Spectral Density (ASD) of the modeled ground translation and ground tilt sensed as translation under low ($0 - 5$ m/s) and high ($10 - 12$ m/s) wind conditions along with various sensor noise models. We assume that the ground translation does not change under different wind conditions, but the increase in the sensed translation is only due to the increased tilt. In reality, the ground motion above $\sim$0.1 Hz increases

slightly with wind speed. Additionally, we assume that the platform and the ground seismometer experience the same amplitude, but incoherent, ground tilts as they are similar distances from the walls of the building. Fig. 6 shows the ground tilt under low wind and high wind conditions.

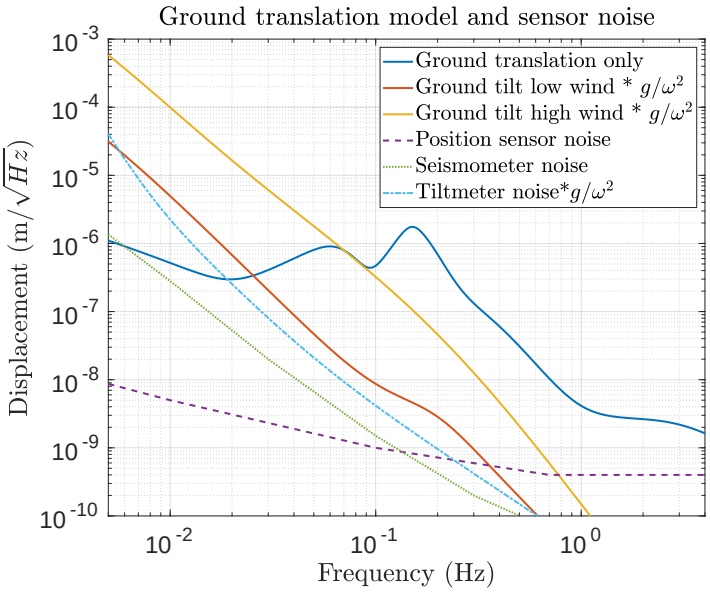

Figure 5. ASD of the modeled ground translation, along with low and high tilt models as sensed by a seismometer. Also shown are translational sensor noise models for the position sensor (CPS), seismometer (T240), and tiltmeter (BRS).

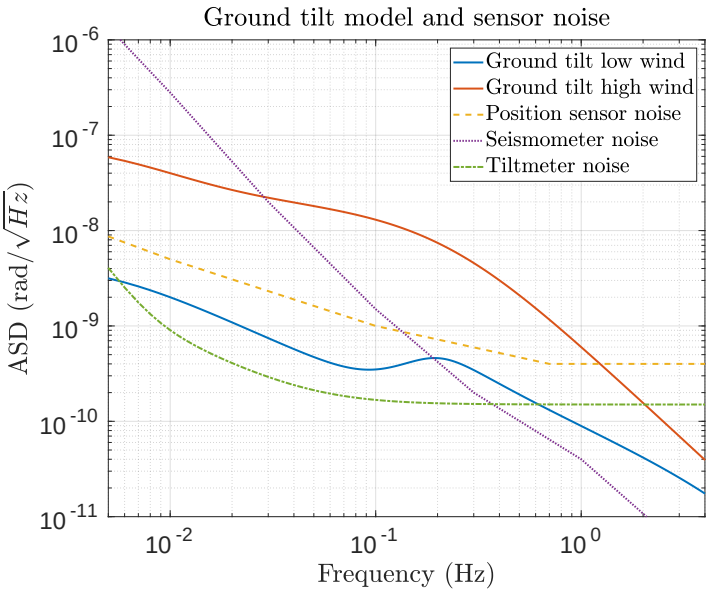

Figure 6. ASD of modeled low and high ground tilt along with tilt sensor noise models for the position sensor (CPS), seismometer (T240), and tiltmeter (BRS).

Using these models and Eqs. 1-7, we can compute the platform responses in translation and tilt for the two control strategies. Fig. 7 shows the platform tilt under low wind conditions with the O1 configuration. The control performance is limited by the position sensor noise below $\sim$ 500 mHz.

Similarly, Fig. 8 shows the translation of the platform under low wind conditions. At frequencies above $\sim$ 0.8 Hz, the platform achieves a nearly sensor-noise-limited isolation performance. At lower frequencies, the translation of the platform is dominated by residual ground motion and is limited by residual signal in the stop band of the low-pass filter. However, as the sensor noise is only a factor of few below the platform motion, the differential motion between platforms located close to each other is nearly sensor noise limited.

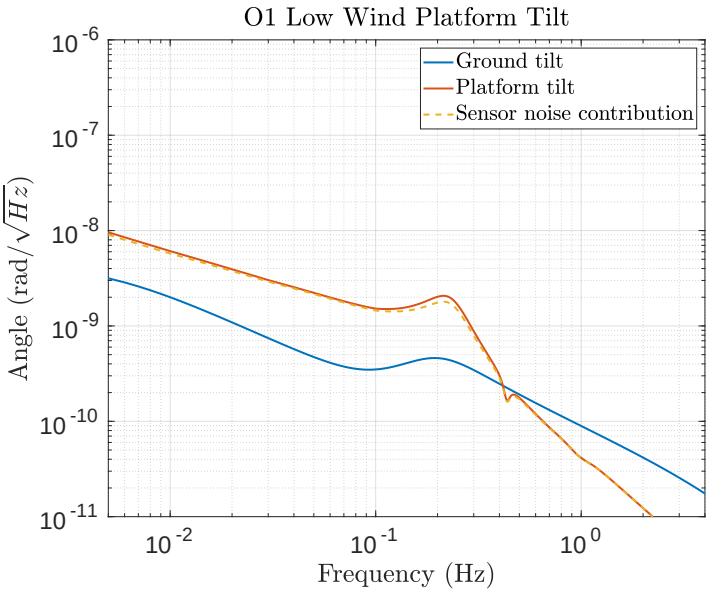

Figure 7. ASD of modeled platform tilt in low wind. Below $\sim$ 500 mHz the control performance is limited by the position sensor noise.

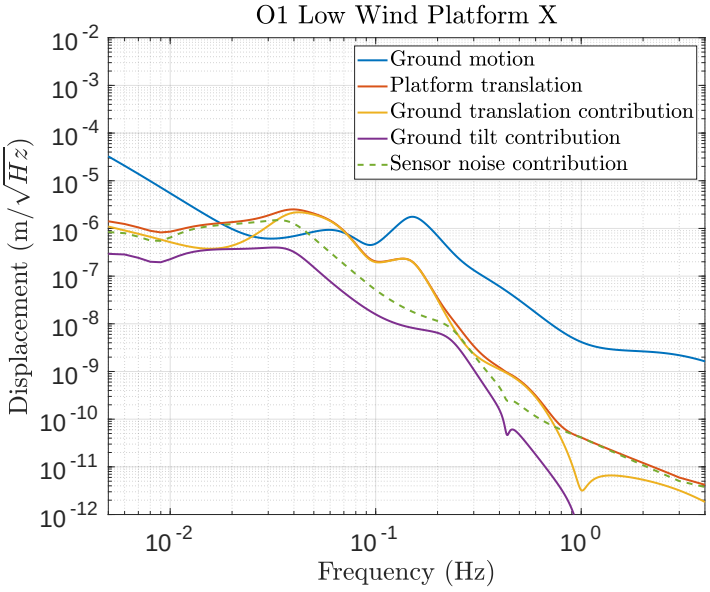

Figure 8. ASD of modeled platform translation during low wind in the O1 configuration. The yellow and purple curves represent, respectively, platform translation caused by ground translations and ground tilts while the red curve represent the residual platform translation.

When wind speeds increase, the ground tilt and consequently the platform tilt increases significantly as shown in Fig. 9. As a result of this increased platform tilt, the platform motion increases by a factor of approximately 20 at 50 mHz as shown in Fig. 10. The increased low-frequency platform translation leads to an increase in the angular motion of the suspended mirrors through length to angle cross-couplings. The increased angular motion is often responsible for the lockloss since the control loops which fight this motion have small bandwidths in order to minimize noise in the gravitational wave band.

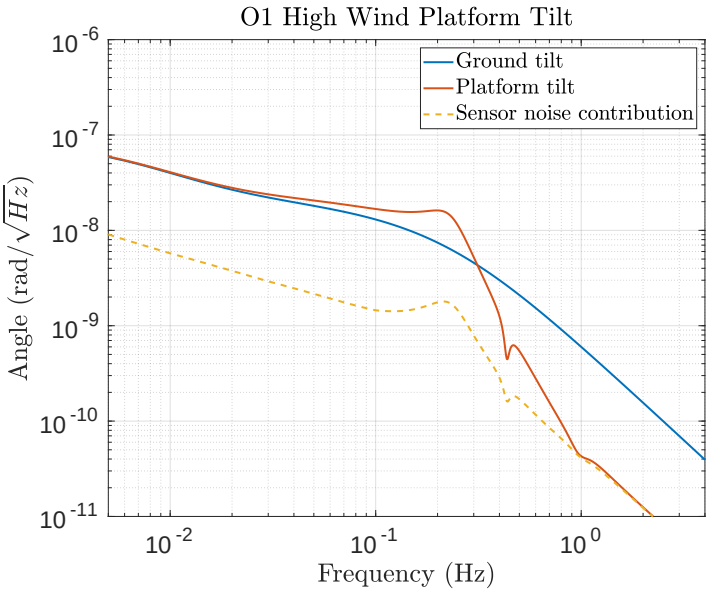

Figure 9. ASD of modeled platform and ground tilt in high wind.

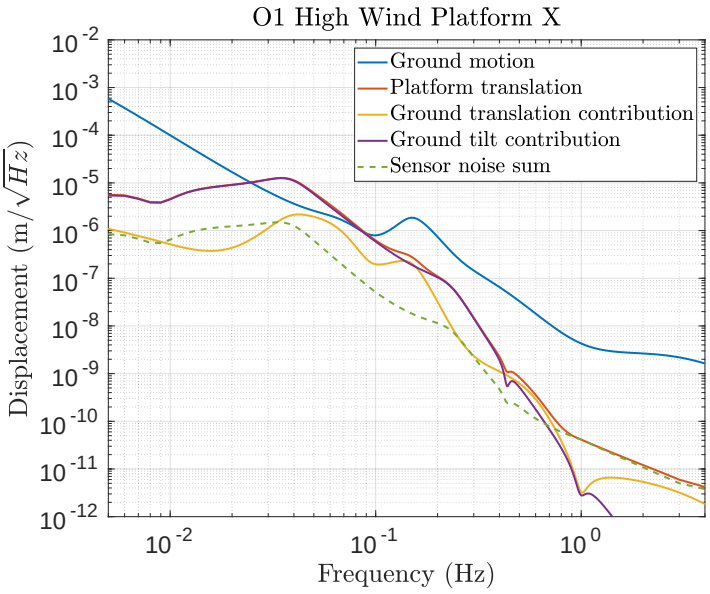

Figure 10. Platform translation in high wind in the O1 configuration.The yellow and purple curves represent respectively platform translation caused by ground translations and ground tilts while the red curve represent the residual platform translation.

In comparison, Fig. 11 shows the platform's translation response under the O2 configuration. Note that the O2 platform tilt response is identical to that in the O1 configuration since the tilt control scheme was not changed. The platform's isolation above 1 Hz and near the microseism is similar as before, but the isolation is degraded between 0.2 to 0.7 Hz. The gain peaking near 60 mHz is also comparable to before. However, the sensor noise contribution, mainly comprised of the position sensor tilt, is suppressed significantly at low frequencies. This configuration has the signficant advantage of the platform motion being dominated by ground motion in this band, which has been found to be mostly common over the 4-km long arms as seen in Fig. 1. Thus, the differential platform motion is reduced to a larger extent.

Fig. 12 shows the platform performance under windy conditions, where the benefit from the tilt sensor is most visible. The tilt contribution to the platform motion is suppressed by more than an order of magnitude in the $20 - 100$ mHz range and the overall platform motion is signficiantly reduced. The ground tilt still dominates the platform motion between $0.2 - 0.4$ Hz due to the lack of a reliable rotation sensor on the platform.

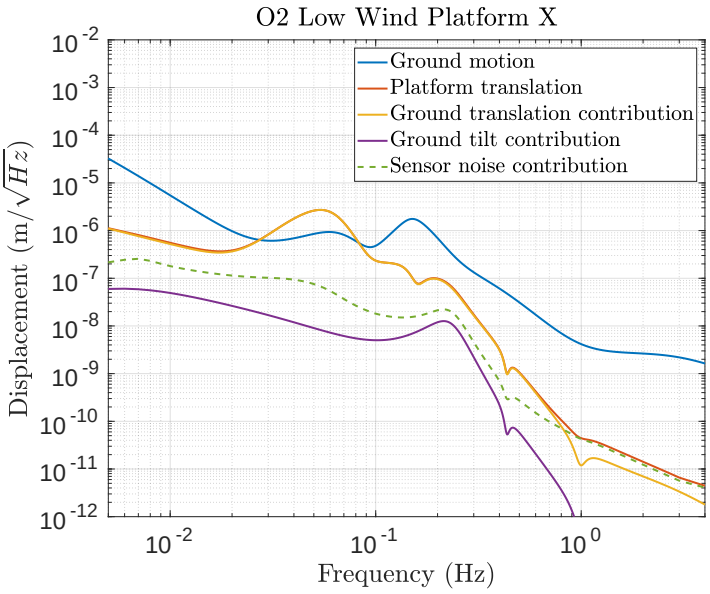

Figure 11. Platform translation in low wind in the O2 configuration.The yellow and purple curves represent respectively platform translation caused by ground translations and ground tilts while the red curve represent the residual platform translation.

3. Comparison with Measured Data

The model in the previous section allows a calculation of the platform motions given the input ground translation and tilts. In reality, we measure ground motion with seismometers, whose signal is a combination of translation and tilt, and ground rotation with the rotation sensors. However, it has been found that while most translations at these frequencies are coherent over large distances, tilts are coherent only over a few meters. This is thought to be due to the local deformation of the observatory floor. Thus, while tilt can be efficiently subtracted from a nearby seismometer, ground tilt measurements cannot be effectively used for feedforward control of the platform rotation. The platforms and rotation sensors are separated by 5-7 meters and physical obstacles did not allow the sensors to be placed closer to the chambers. Additionally, the platform tilt is a combination of those experienced by its four widely spaced legs.

Despite these issues, the seismic isolation of the platforms was improved by using the tilt-subtracted ground translation signal. To test the model, we compare the predictions against measured platform motions during O2. Fig. 13 shows the measured and modelled platform tilt during windy conditions during O2. The first two curves are the measured T240 and CPS tilt sensors on the platform, which show the isolation above the blend frequency of $\sim$ 250 mHz. The next two curves show the predictions of the model based on the measured ground tilt. The qualitative agreement is quite good, differing by less than a factor of $\sim$2-3 at most frequencies, given that we expect there to be differences between the measured ground tilt near the rotation sensor and

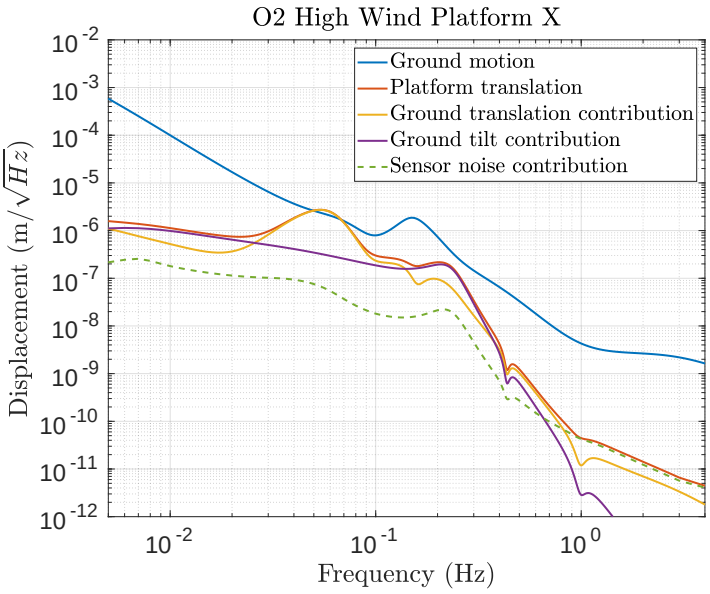

Figure 12. Platform translation in high wind in the O2 configuration. The yellow and purple curves represent respectively platform translation caused by ground translations and ground tilts while the red curve represent the residual platform translation.

the tilt near the test mass chamber.

Similarly, Fig. 14 shows the measured and modelled platform translation during windy conditions in O2. As before, the first two curves are the measured T240 and CPS translation sensors on the platform, which show the isolation above the blend frequency of ~ 250 mHz and the extra isolation due to the sensor correction at lower frequencies. The next two curves show the predictions of the model based on the measured ground translation and tilt. Once again, the qualitative agreement is quite good.

4. Filter tuning and performance measurements

For the beam rotation sensor to be used most effectively, the tilt signal, corrected for its effect on translation, should simply be subtracted from the ground seismometer. However, there are several effects that can spoil the total performance: a calibration difference between the ground seismometer and the BRS, the self-noise of the BRS at low frequencies, the mechanical response of the BRS, and the natural AC-coupling of the seismometer. Fortunately each of these effects is largely independent of the others, thus they could be optimised individually.

The figure of merit for optimising the tilt-subtraction was the cumulative RMS velocity, integrated from high-frequencies to low-frequencies, of the tilt-corrected seismometer signal. There are a number of reasons for selecting the RMS velocity. First, it is an integrated measure of the spectrum, which clearly displays whether a small improvement at some frequencies is worth some degradation at other frequencies.

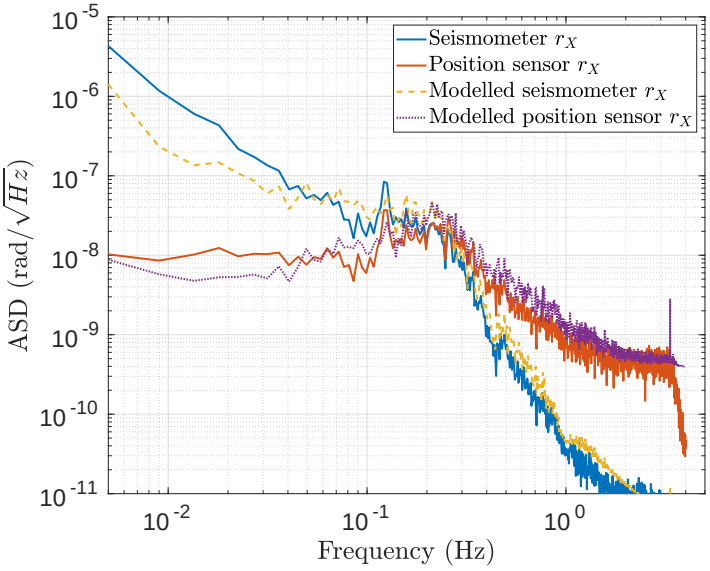

Figure 13. Comparison of measured platform tilt to modelled tilt in high wind in the O2 configuration.

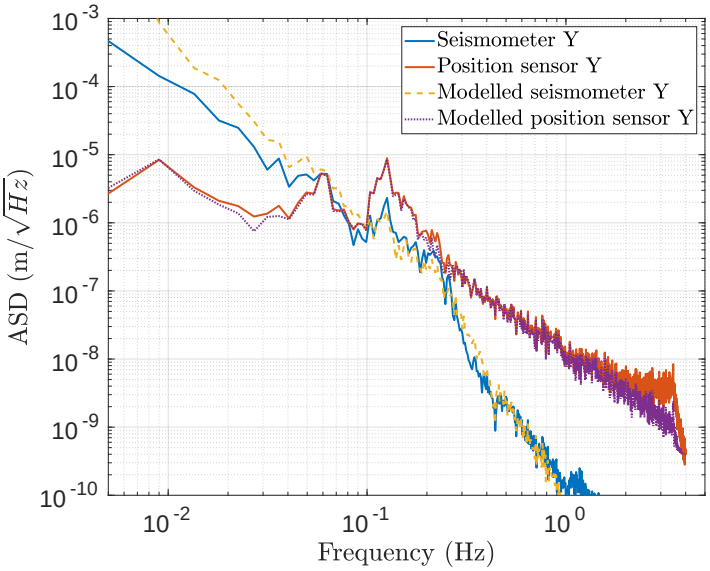

Figure 14. Comparison of measured platform translation to modelled translation in high wind in the O2 configuration.

Second, the velocity determines key interferometer behaviours such as the coupling of

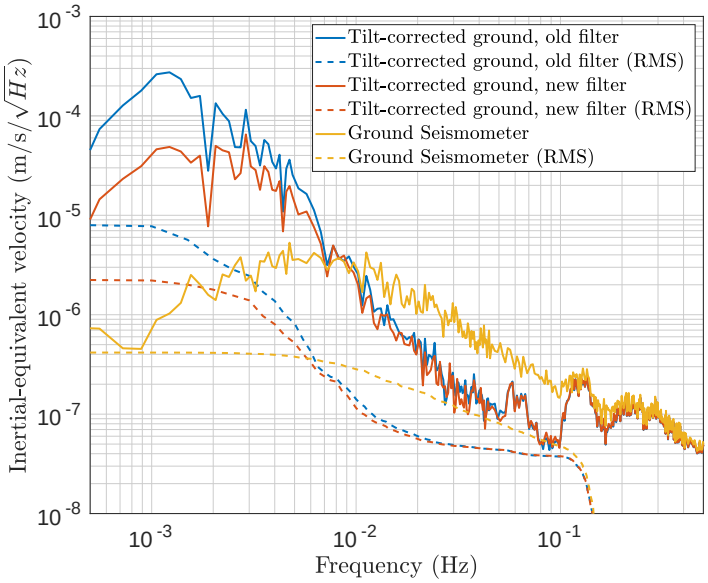

Figure 15. The impact of optimising the tilt-subtraction filter. After turning, the tilt subtraction is very slightly improved, limited by the coherence of the tilt motion at the sensors, and at low frequencies the self-noise injection from the BRS is reduced by a factor of nearly 4 in RMS.

scattered light. Third, the RMS converges by approximately 1 mHz, allowing a firm quantification of low-frequency noise injection.

The tilt subtraction tuning was performed using a time-segment of 5-hours with moderate wind. The tilt-subtraction filter was applied to the BRS data, and the output subtracted from the seismometer signal. Each component of the filter was optimised independently in a grid-search. Figure 15 shows the improvement in performance after the tilt-subtraction filter was optimised. The dominant effect was matching the high-pass filter applied to the BRS with the AC-coupling filter in the seismometer. This both reduced the low-frequency noise injected by the BRS by a factor of approximately 4, and improved the phase-matching between the signals near 10 mHz, slightly improving tilt-subtraction. The resulting filter was implemented and tested on new stretches of data, with similar effect.

To quantify the downstream effect of tilt-subtraction on the motion of LIGO's isolated platforms, the CPS translation sensors are used as a measure of low-frequency motion. This approximation is valid for frequencies between 1 mHz and approximately 0.1 Hz. As previously, we look at spectral density and cumulative RMS of the velocity. Using this metric, the sensor-correction filter was tuned in a similar manner to the tilt-correction filter. There are many highly-coupled parameters in the sensor-correction filter, so it was not possible to grid-search for a global minimum, but the performance was slightly improved.

To make the measurement more directly applicable to the complete interferometer, we also look at the difference between the 4 km separated CPS signals, synthesising the spectral density of the arm-length fluctuations. Figures 16 and 17 show the effect

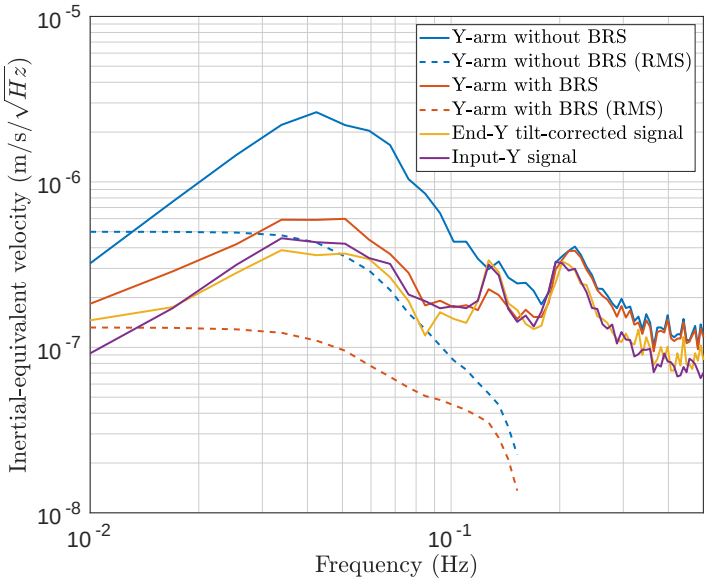

Figure 16. The effect of BRS on the differential-velocity of the platforms in one of LIGO's arms during a period of high wind. The data was recorded over a 2-hour period when the wind speed averaged approximately 10 m/s. The figure of merit is the Y-arm differential velocity when using the BRS (black dashed line) compared with the non-BRS case (dashed red line). The RMS is accumulated starting from 0.15 Hz, indicated by the dashed vertical line.

of the tilt-subtraction on the rate-of-change of the length of the Y-arm for high and low wind conditions respectively. For the high-wind case, the RMS velocity between the ISI platforms was reduced by a factor of 3.7. Interestingly, the differential velocity is lower than either of the individual velocities at the small peak near 0.13 Hz, which is strong evidence for common-mode rejection of ground-translation after the tilt-subtraction process. For the low-wind case we see that the BRS adds no additional noise to the platform. The X-arm tilt-subtraction reduced the RMS velocity even further, by a factor of approximately 5, and the noise injection was similarly negligible during low winds.

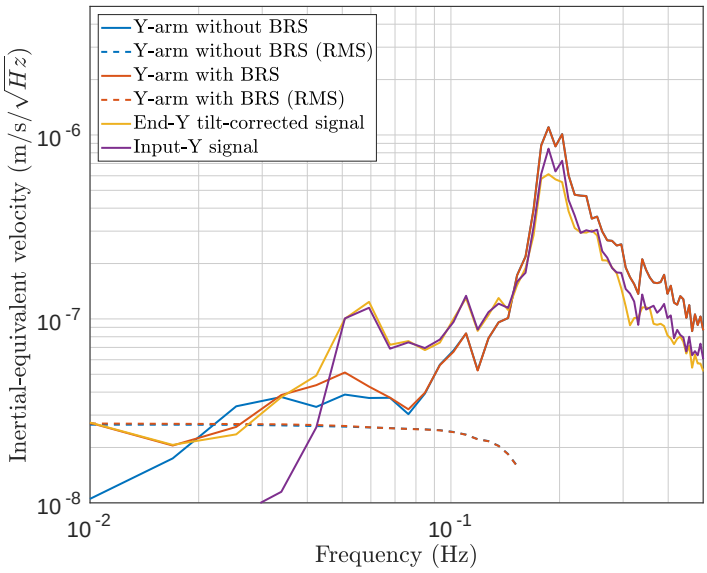

Figure 17. The same sensors as in Fig. 16, but for a 2-hour stretch with wind speeds of 1 m/s. The two RMS curves are almost identical, proving that even in the lowest wind conditions, the BRS does not degrade performance or effect the common-mode rejection of translation.

5. Impact on Duty-Cycle and noise

As expected, the reduced platform motion under windy conditions has been anecdotally observed to make lock acquisition easier. The impact of the O2 configuration on the duty cycle can be assessed by evaluating the fraction of the time the interferometer was in the locked state as compared to the unlocked state, for a given wind speed. Histograms of the locked fraction are shown in Fig. 18 for the O1 and O2 configurations. The improvement to the duty cycle in O2 is evident above 5-7 m/s winds. It is also interesting to note that the locked fraction appears to drop nearly linearly with wind-speed in O1 configuration, whereas in O2 it is nearly independent of wind-speed up to about 15 m/s, after which it falls off linearly due to residual tilt contamination. Decreases in duty cycle at low wind speed are due to differences in the observatory conditions between O1 and O2 that are independent of the seismic isolation scheme.

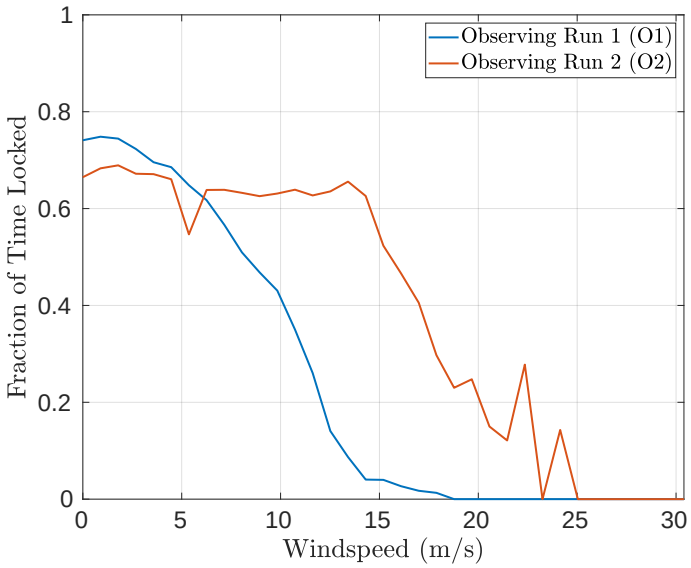

Figure 18. Histogram of fraction of the time the interferometer was locked as a function of wind speed for the O1 and O2 configuration.

6. Summary

The paper discusses the effect of ground tilt on active seismic isolation in LIGO. We have presented a simple analytical model to compare the impact of tilt on platform motion in two configurations and have shown the benefit of using a ground rotation sensor. This model shows qualitative agreement with measurements of the platform motion. The use of the ground-rotation-sensors has made the active isolation system less vulnerable to wind-induced tilt and improved the duty cycle of the LIGO Hanford Observatory significantly during wind speeds exceeding 7 m/s. Similar duty cycle improvements are expected to accompany the recent installation of ground rotation sensors at the LIGO Livingston Observatory. In the near future, the installation of on-platform compact-BRSs, which are currently in development, may decrease the tilt motion of the isolation platforms and further increase the performance of the low-frequency isolation.

7. Acknowledgements

The authors would like to thank Robert Schofield for his valuable comments. This work was carried out at the Laser Interferometer Gravitational-Wave Observatory (LIGO) Hanford Observatory (LHO) by members of LIGO laboratory and the LIGO Scientific Collaboration including University of Washington, Seattle, University of Birmingham, Standford University, and Massachusetts Institute of Technology. LIGO was constructed by the California Institute of Technology and Massachusetts Institute of Technology with funding from the National Science Foundation (NSF) and operates under Cooperative Agreement PHY-0757058. Advanced LIGO was

built under Award PHY-0823459. Participation from the University of Washington, Seattle, was supported by funding from the NSF under Awards PHY-1607385, PHY-1607391, PHY-1912380, and PHY-1912514. Participation from Stanford University was supported by funding from the NSF under Award PHY-1708006.

8. References

[1] Abbott B P *et al.* (LIGO Scientific Collaboration and Virgo Collaboration) 2016 *Phys. Rev. X* **6**(4) 041015 URL `https://link.aps.org/doi/10.1103/PhysRevX.6.041015`

[2] Abbott B P *et al.* (LIGO Scientific Collaboration and Virgo Collaboration) 2016 *Phys. Rev. Lett.* **116**(13) 131103 URL `https://link.aps.org/doi/10.1103/PhysRevLett.116.131103`

[3] Venkateswara K, Hagedorn C A, Gundlach J H, Kissel J, Warner J, Radkins H, Shaffer T, Lantz B, Mittleman R, Matichard F and Schofield R 2017 *Bulletin of the Seismological Society of America* **107** 709–717

[4] Longuet-Higgins M S 1950 *Philosophical Transactions of the Royal Society of London A: Mathematical, Physical and Engineering Sciences* **243** 1–35 ISSN 0080-4614 (*Preprint* `http://rsta.royalsocietypublishing.org/content/243/857/1.full.pdf`) URL `http://rsta.royalsocietypublishing.org/content/243/857/1`

[5] Matichard F *et al.* 2015 *Classical and Quantum Gravity* **32** 185003 URL `http://stacks.iop.org/0264-9381/32/i=18/a=185003`

[6] Venkateswara K, Hagedorn C A, Turner M D, Arp T and Gundlach J H 2014 *Review of Scientific Instruments* **85** 015005 (*Preprint* `http://dx.doi.org/10.1063/1.4862816`) URL `http://dx.doi.org/10.1063/1.4862816`

[7] Lantz B 2008 *LIGO DCC*

Appendix A.

The two commonly used blend filters are shown in Fig. A1 and A2, labelled as 250 mHz and 45 mHz blends. The sensor correction filter used in O2 is shown in Fig. A3.

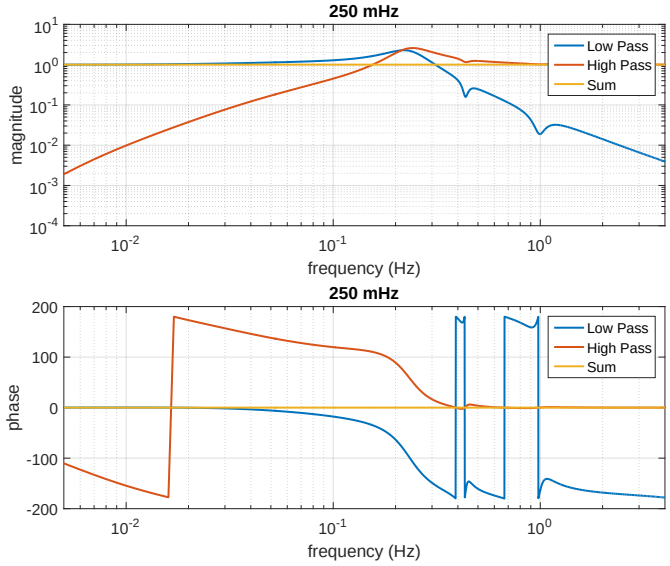

Figure A1. 250 mHz blend filters.

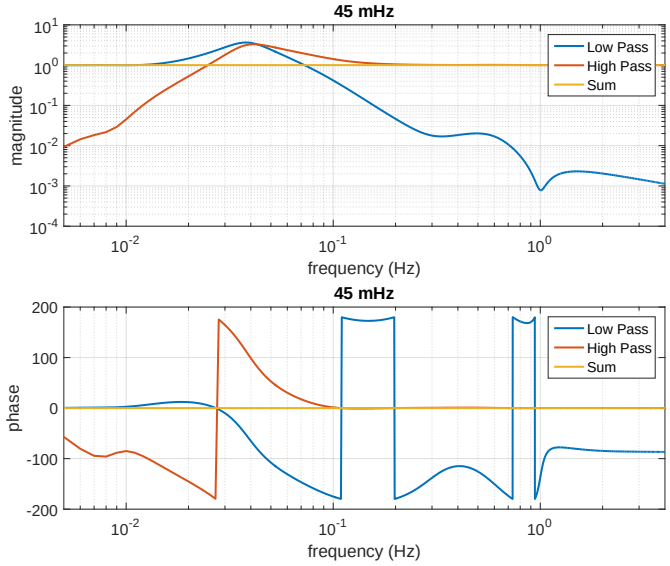

Figure A2. 45 mHz blend filters.

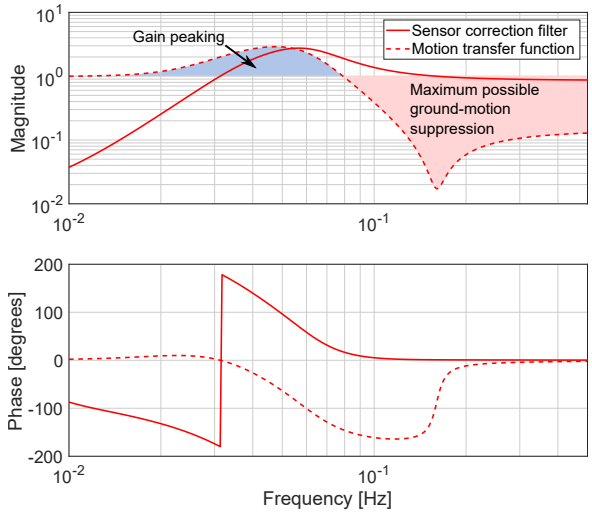

Figure A3. Sensor correction filter showing the maximum possible groun-motion suppression.